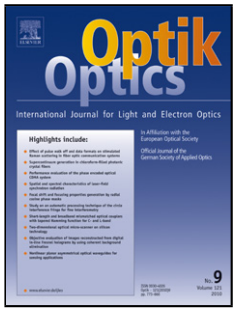

Neural network based synthetic aperture ladar imaging through marine atmosphere

Tianan Lu, Fei Huang, Hongping Li

PII: S0030-4026(20)30811-1

DOI: https://doi.org/10.1016/j.ijleo.2020.164975

Reference: IJLEO 164975

To appear in: *Optik*

Received Date: 6 February 2020

Revised Date: 19 May 2020

Accepted Date: 20 May 2020

Please cite this article as: Lu T, Huang F, Li H, Neural network based synthetic aperture ladar imaging through marine atmosphere, *Optik* (2020), doi: https://doi.org/10.1016/j.ijleo.2020.164975

Neural network based synthetic aperture ladar imaging through marine atmosphere

Tianan Lu[a]*, Fei Huang[a,b], Hongping Li[c]

a Physical Oceanography Laboratory, Ocean University of China, Qingdao 266100, China

b Qingdao National Laboratory for Marine Science and Technology, Qingdao 266100, China

c College of Information Science and Engineering, Ocean University of China, Qingdao 266100, China

Abstract

The atmospheric turbulence can severely affect the azimuth imaging of the Synthetic Aperture Ladar (SAL). Based on a neural network, this study generates atmospheric phase screens complied with marine atmosphere spectrum. The SAL imaging results with different turbulence intensities and laser wavelengths are calculated, and the changing law of the ratio of real aperture length to atmospheric coherence diameter with turbulence intensity under different slant ranges and laser wavelengths are analyzed in this paper. The results suggest that the SAL imaging becomes worse as the turbulence intensity is stronger, and even the target is not able to be distinguished. A longer laser wavelength can be used to alleviate the defocus effect, and the phase error compensation algorithm based on marine phase screens can effectively improve the SAL imaging quality to guarantee the real–time process of echo signals of SAL in the marine atmosphere.

Key words: synthetic aperture ladar; marine atmosphere; phase screen; neural network

1.Introduction

Synthetic Aperture Ladar (SAL) is an optical imaging radar with a radiation source of laser. Since the wavelength of laser signal is shorter and propagation frequency is higher than that used in Synthetic Aperture Radar (SAR), it is able to yield larger Doppler frequency shift for a target with the same relative velocity. Compared with SAR, it has significant advantages in terms of imaging time and resolution, and it overcomes the shortages of thin scanning beam and small detecting area of normal imaging ladars, becoming a focus issue of imaging ladar recently[1-6]. Atmospheric absorption and atmospheric turbulence are the main environmental factors to affect SAL imaging. The refractive fluctuation and variation of atmospheric density causes the wavefront distortion of laser due to atmospheric turbulence, which can further destroy the coherence of laser beam, leading to a defocus effect on the imaging of SAL. For the influence of atmospheric turbulence on SAL, Karr studied the effect of atmospheric turbulence on SAL imaging resolution[7]. Schumm and Dierking demonstrated the integrated effects of turbulence on SAL imaging[8]. Depoy and Shaw used model-based atmospheric phase correction method to overcome atmospheric phase errors in SAL data[9]. Lucke simulated the influence of atmospheric turbulence on one dimensional SAL imaging quality based on phase screens[10]. Phase screen is still an useful methodology to stimulate the atmospheric effect on optical propagation systems[11-15]. In addition, the effect of marine atmosphere on beam propagation is evident[16-18]. Recently, many kinds of Convolutional Neural Network (CNN) are employed in plenty of orbital angular momentum and atmospheric turbulence model studies[19-22]. Some related work for marine research such as cognitive marine radar, cost-effective optical sensor in

marine environment and tracking multiple marine ships via multiple sensors has been studied[23-25]. Hence, the effectiveness of improvement of neural network based marine atmospheric phase screens on SAL imaging needs to be further examined. For this purpose, this paper is organized as follows: Section 2 is to propose a neural network based marine atmospheric phase screen generation method. Section 3 introduces the adopted improved phase error compensation method. Section 4 presents relevant SAL imaging results and numerical analysis. Section 5 is the conclusion.

2.Neural network based marine atmospheric phase screen

The key to simulate atmospheric turbulence based on phase screens is transferring the influence of turbulence on optical waves to a set of thin screens, i.e., phase modulation. The wave front of optical waves in turbulent atmosphere can be expressed as

$$D(r_1, r_2) = < [\varphi(r_1) - \varphi(r_2)]^2 > \tag{1}$$

where $\varphi(r_1)$ and $\varphi(r_2)$ are the sample phases of r_1 and r_2,respectively. $<\cdot>$ denotes the mean value and $D(r_1, r_2)$ denotes the structure function. For a local homogeneous isotropic turbulence, the power spectrum of marine atmospheric turbulence can be written as

$$\Phi_n(\kappa) = 0.033 C_n^2 (1 - 0.061\kappa / \kappa_H + 2.83\kappa^{7/6} / \kappa_H^{7/6}) \times (\kappa^2 + \kappa_0^2)^{-11/6} \exp(-\kappa^2 / \kappa_H^2) \tag{2}$$

where $\kappa_H = 3.41 / l_0$, $\kappa_0 = 1 / L_0$, and l_0 and L_0 are the inner scale and outer scale of turbulence, respectively[16]. C_n^2 is the refractive index structure constant, which is written as

$$C_n^2 = (0.423 k^2 r_0^{5/3} L)^{-1} \tag{3}$$

where k is the wave number, r_0 is the atmospheric coherence length, L is the integrated length of turbulent path[26]. The phase screen generation method we adopt in this study is based on Monte-Carlo random factor[27]. After each expansion, those points neglected to expand will not be chosen in subsequent growth. If assume (x_0, y_0) is the initial expansion point, the phase screen expression is written as

$$\varphi_0(x, y) = \varphi_0(x_0, y_0) + R_a \sqrt{D(r) + R\sigma_D^2} \tag{4}$$

where R_a is the random number of 0 or 1. $D(r)$ is the mean square phase difference of a distance of r between two points. R is the Monte-Carlo random factor between 0 and 1 with uniform distribution. σ_D^2 is the phase fluctuation variance of the real aperture, which can be expressed as

$$\sigma_D^2 = 1.0299 (D / r_0)^{5/3} \tag{5}$$

where D denotes the real aperture length. Since the initial point must be chosen, at the first

expansion, R_a needs to be set as 1. From the second expansion, R_a can be alternated. The first-layer phase screen is generated when the point number satisfy the gird number. In order to establish the marine atmospheric numerical model, multi-layer phase screens are used in this paper to stimulate the statistical characteristics of the turbulent integrated path, and those phase screens are not independent completely. The relevance is connected by the initial phase value. This value is set in accordance with the value at the same position in last phase screen. Multi-layer phase screen generation expression is written as

$$\varphi_N(x,y)=\varphi_{N-1}(x,y)+R_a\sqrt{D(r)+R\sigma_D^2},N\geq 1 \tag{6}$$

where N denotes the number of layer. The spacing between two neighboring phase screens over the integrated path is in accordance with the refractive index fluctuations[28], which can be expressed as

$$\delta_I^2(L)=1.23C_n^2\kappa^{7/6}L^{11/6} \tag{7}$$

If the turbulence intensity is weak, that makes the refractive index fluctuation over the whole integrated path less than 0.1, the number of phase screens is set as 10. If the turbulence intensity is relatively strong, we can increase the number to decrease the refractive index fluctuation between spacing to $\delta_I^2(\Delta L)<0.1$. ΔL denotes spacing length. Theoretically, the more phase screens we generate, the better result we obtain, while computational burden needs to be taken into account.

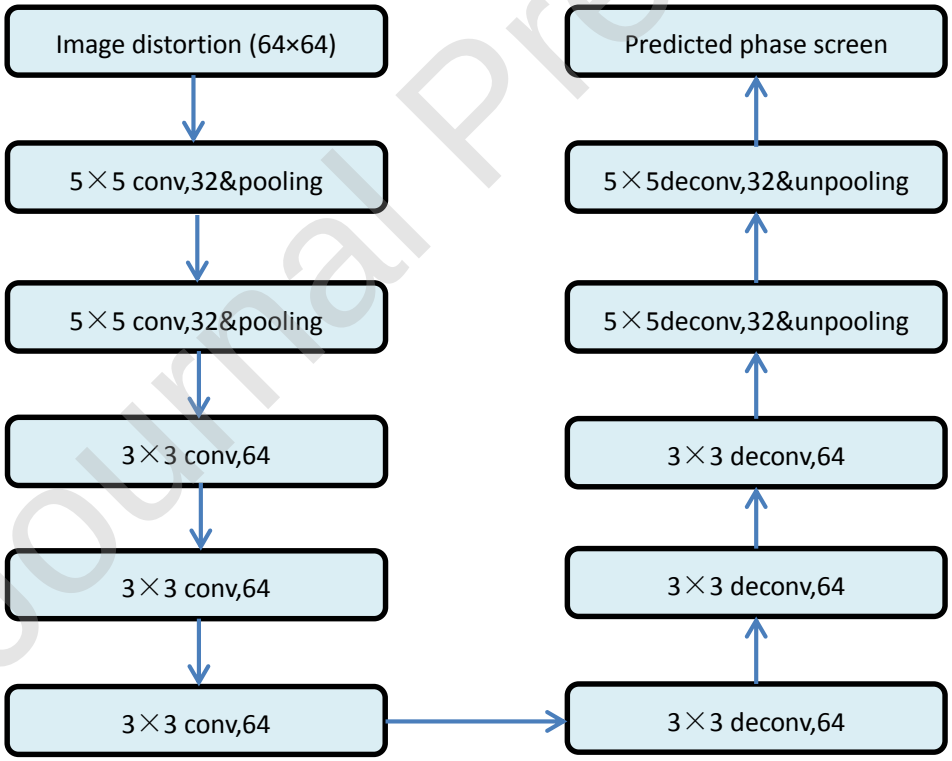

Fig.1. CNN schematic diagram

To better simulate the atmospheric effect and compensate the SAL phase errors, a kind of

deep learning approach called CNN is adopted in this article. The CNN is aiming at learning the phase modulation of marine atmosphere based on phase screens. As shown in Fig.1, it has 5 convolution (conv) layers and 5 deconvolution (deconv) layers. The convolution filters have 32 kernels in two convolution layers of size 5 × 5 with pooling (sampling method) and 64 kernels of the rest. Likewise, the deconvolution layers have a similar structure. The input is the SAL image distortion with a resolution of 64×64. The distortion means the difference between the original SAL image without turbulence and the image with it. The output is the phase perturbations from SAL signal propagation, i.e., phase screens. To train our neural network, we prepare 10000 SAL images with atmospheric effect. 90% of which are used for training and the rest of them used for validation. After training, another 1000 SAL images are generated to test the effectiveness.

3.Phase screen based phase error compensation

The Rank one phase estimation autofocus algorithm based on an assumption that one or more scatter points in a single range direction unit[29]. After dechirp, the echo signals in range units consists of signals with different frequencies and amplitudes. Through Fourier transformation, we can obtain frequency spectrum. Adding window on scatter points in azimuth direction, and the point with strongest energy is selected. The discrete compressed echo data in range direction can be written as

$$s_r(m,n) = A_{m,n} \exp\left\{ j\left[\varphi_{0,n} + 2\pi f_{m,n} m + \varphi_c(m,n) \right] \right\} \tag{8}$$

where $A_{m,n}$, $\varphi_{0,n}$, $f_{m,n}$, $\varphi_c(m,n)$,m,n are echo amplitude, initial phase value, Doppler frequency, phase error, sample point in range direction, and sample point in azimuth direction, respectively. Since the point values in SAL echo range units are not large enough, the maximum value in a range unit needs to be selected according to the complex amplitude. The methodology in this study is shifting the center to the maximum point, and applying window function to it. Window function is the key to improve the robustness of the autofocus algorithm. A proper window length contributes to reduce the estimation deviation. If the window length is too long, the signal-to-noise ratio in the imaging processing area in lower. If the window length is too short, the lack of the capture of defocus area will cause the distortion of phase error estimation. The value of the window length has a fundamental impact on the computational efficiency and estimation accuracy of the algorithm. When the center is shifting, the pulse energy is accumulating. The pulse energy distribution function can be expressed as

$$s(x) = \sum_n \left| f_n(x) \right|^2 \tag{9}$$

After the shift, the energy is centered at S(0), the window length then set as a synthetic aperture length. Assuming $s_r^{'}(m,n)$ is the shifted signal in range direction, the differential signal can be expressed as

$$D(m,n) = s_r^{'}(m+1,n) s_r^{'}(m,n) = \left| A^2 \right| \exp\left\{ j\left[2\pi f_{m,n} + \Delta\varphi_c(m,n) \right] \right\} \tag{10}$$

where $\Delta\varphi_c(m,n) = \varphi_c(m+1,n) - \varphi_c(m,n)$. The two parameters to be estimated are $f_{m,n}$ and $\Delta\varphi_c(m,n)$, which are written as

$$f_{m,n}^{(p)} = \frac{1}{2\pi}\arg\sum_{n=1}^{N} D(m,n)\exp\left[-j\Delta\varphi_c^{(p)}(m,n)\right] \tag{11}$$

$$\Delta\varphi_c^{(p)}(m,n) = \arg\sum_{n=1}^{N} D(m,n)\exp\left[-j2\pi f_{m,n}^{p-1}\right] \tag{12}$$

where p denotes the iteration times. Before iterative process, a grid with initial values ($\Delta\varphi_c^{(0)}(m,n)$) in accordance with the number of marine turbulent phase screen is generated. Substituting it into equation, $f_{m,n}^{(0)}$ is obtained. After complex conjugate operation and complex multiplication, i.e., phase error compensation, the compensated echo signal $s_{rc}(m,n)$ can be written as

$$s_{rc}(m,n) = s_r(m,n)\cdot\exp\left\{j\left[-\varphi_c(m,n)\right]\right\} \tag{13}$$

Through the analysis above, two shortages of ROPE, i.e., limitation of model based and uncertainty of preset, have been improved. This study uses window adding and marine phase screens to initialize the iteration process, which makes the algorithm inconsistent with ROPE model is able to estimate the errors with any order, and the shift of frequency spectrum makes the nonlinear iterative initialization more accurate. Therefore, the algorithm improves the capability of autofocus of ROPE and then imaging quality is enhanced. Phase Gradient Autofocus (PGA) is not able to estimate the phase error when phase error changes dramatically, and the linear item brought by PGA itself leads to an imaging shift due to the characteristics of linear unbiased minimum variance estimation[30-32]. The ROPE algorithm based on marine phase screens can overcome similar limitations and eliminate the linear item effect.

4.Results

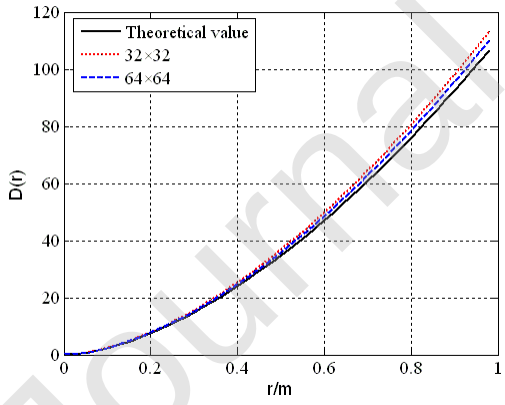

Fig.2. Phase structure function with different grid numbers

The default parameters used in this study are set as followings: radiation source wavelength is 1 μm, $C_n^2 = 1.0\times10^{-16} m^{-2/3}$, resolutions of range and azimuth are 0.01m, inner scale and outer scale are 1 mm and 32 m, respectively. The result of structure function with different grid numbers is shown in Fig.2. Monte-Carlo random factor method overcomes the shortage of deficiency of low-frequency component. As the grid number increases, the high-frequency component and theory value are nearly the same, exhibiting the characteristics of small scale.

Considering the computational efficiency of neural networks, the grid number is 64×64 in this study. In addition, the computational complexity of our system is $O(N^3 \log N)$. If the parameters of the equipment are chosen as 2.5 GHz Intel(R)i5 (CPU) and 8G (memory) with a software of MATLAB, the processing time of 32×32 and 64×64 phase screens are 0.02 and 0.05 second, respectively. Supposing that the airborne SAL platform is operating in a theoretical condition, the slant range between the platform and targets is 10000m, and cruise speed is 100 m/s. The imaging results of spotlight mode under different marine atmosphere are shown in Fig.3.

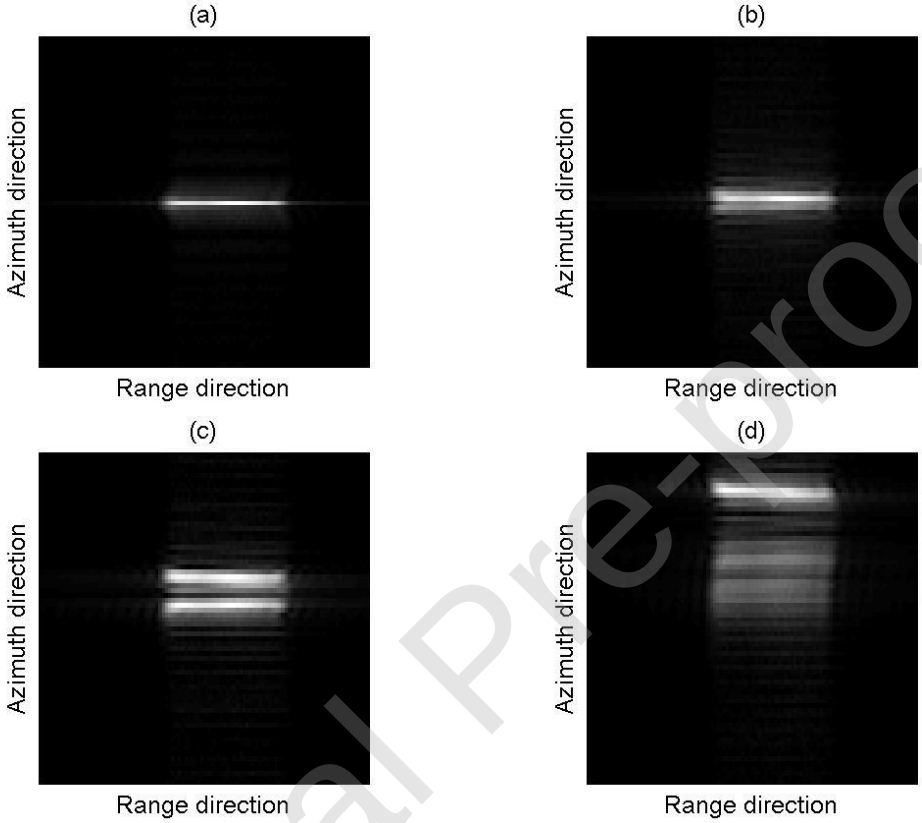

Fig.3. SAL imaging with different turbulence intensities (a) $C_n^2 = 0\mathrm{m}^{-2/3}$ **(b)** $C_n^2 = 1.0\times10^{-18}\mathrm{m}^{-2/3}$ **(c)** $C_n^2 = 1.0\times10^{-16}\mathrm{m}^{-2/3}$ **(d)** $C_n^2 = 1.0\times10^{-14}\mathrm{m}^{-2/3}$

Fig.3(a) is the imaging result without turbulence. The focusing process is favoring. From Fig.3(b) to Fig.3(d), as the intensity increases, defocus effect becomes more severe. Eventually, the imaging target can not be distinguished.

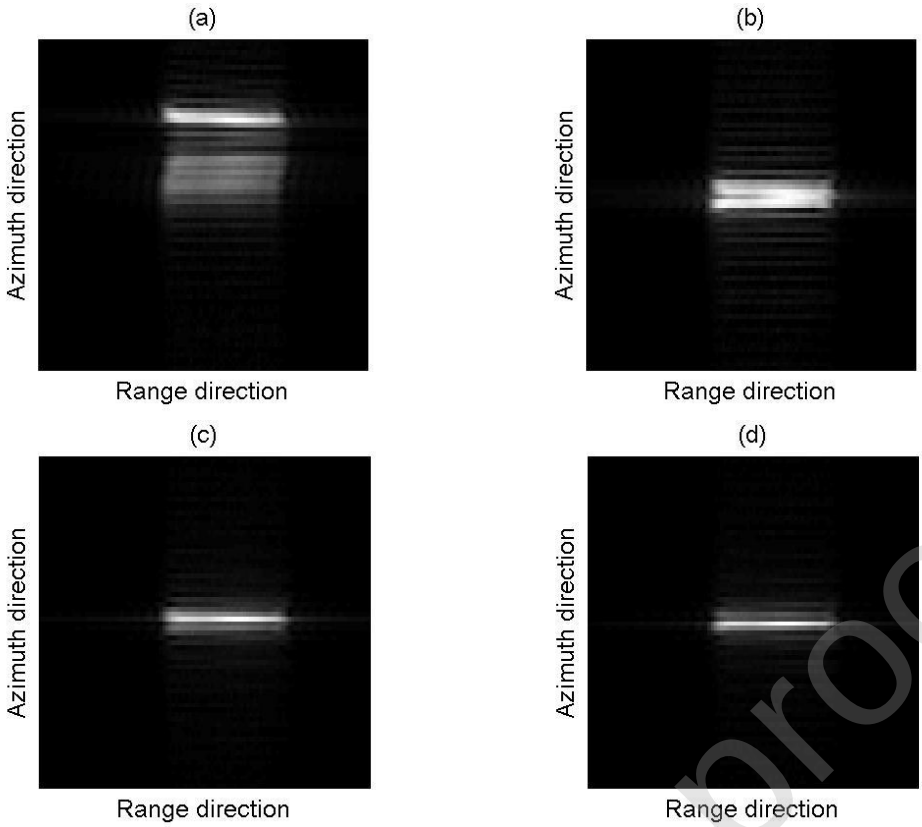

Fig.4. SAL imaging with different wavelengths (a) 1μm (b) 2μm (c) 6μm (d) 12μm

Fig.4 is the SAL imaging results under the conditions of different wavelengths. With the increase of the wavelength, the image becomes clear gradually, which indicates that the longer wavelength has anti-interference performance of turbulence.

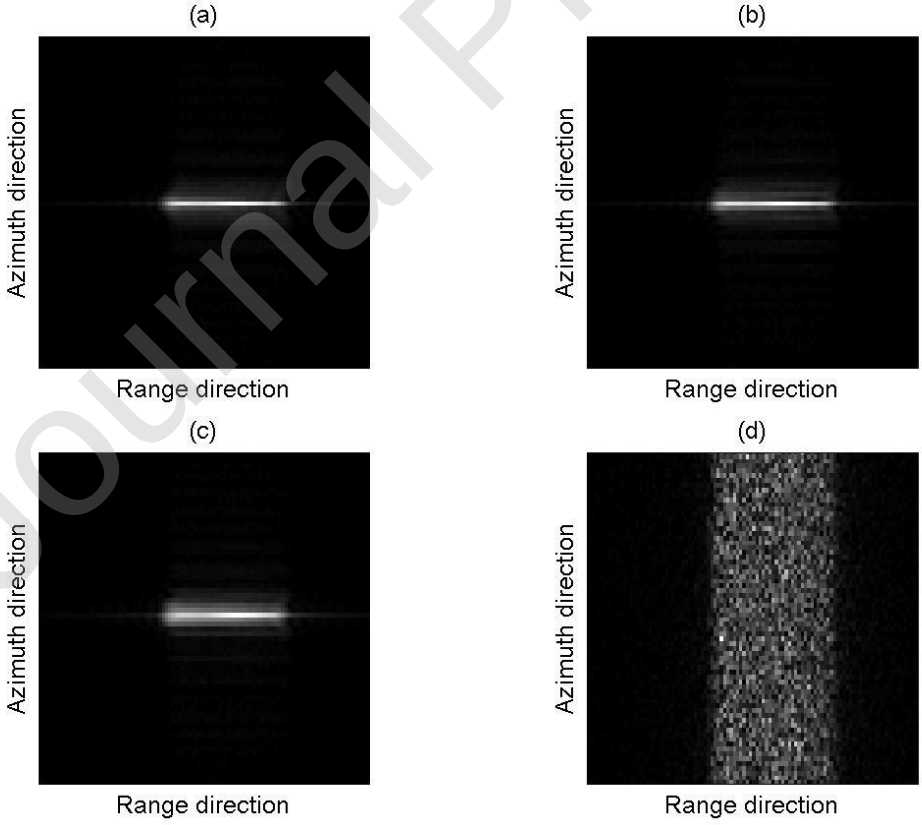

Fig.5. SAL imaging under different weather conditions (a) sunny (b) rainy (c) windy (d) foggy

Fig.5 shows the imaging results based on different weather. Fig.5(a) denotes good weather, while the SAL can easily focus in the rain, whereas when it breezes, slight defocus effect emerges. However, for the foggy days, the target can not be synthesized due to the characteristic of laser.

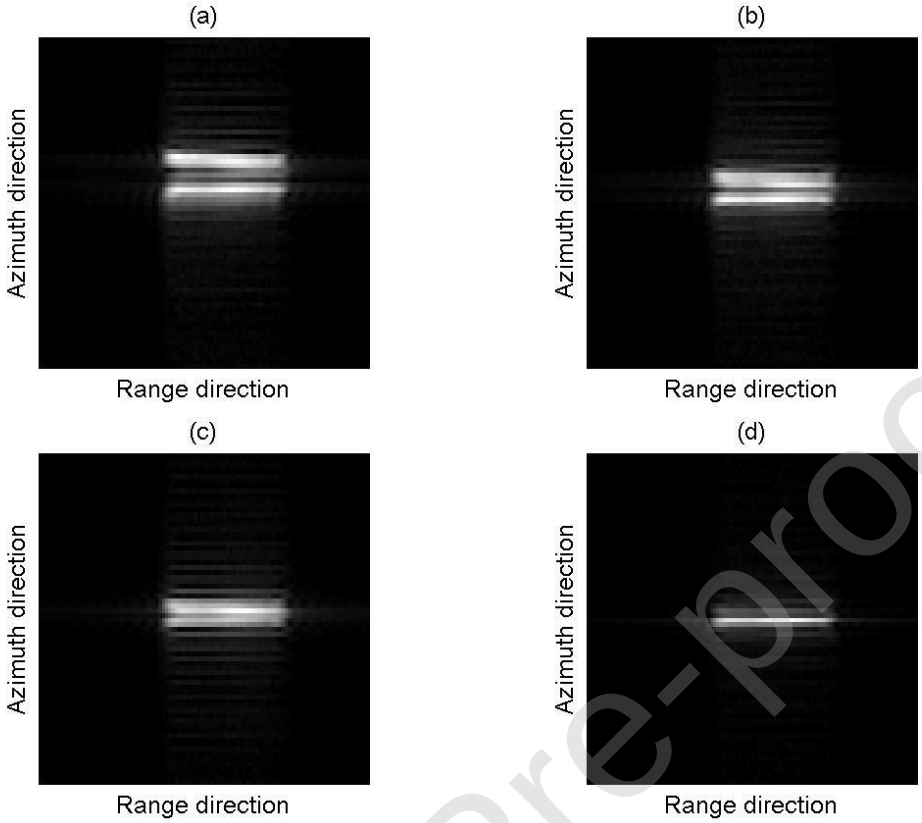

Fig.6. SAL imaging above sea and land and compensation results without and with CNN above sea

Fig.6(a) and Fig.6(b) are the imaging results through marine atmosphere and Kolmogorov atmosphere under an intensity of $C_n^2 = 1.0 \times 10^{-15} \mathrm{m}^{-2/3}$ above land with a probe of longer wavelength of 2μm. Similar to previous studies, the imaging result is better based on long-wavelength laser. Subsequently, iterative phase error compensations are imposed on echo signals for Fig.6(a). As shown in Fig.6(c) and Fig.6(d), the compensation method based on neural networks is able to significantly improve the compensation quality.

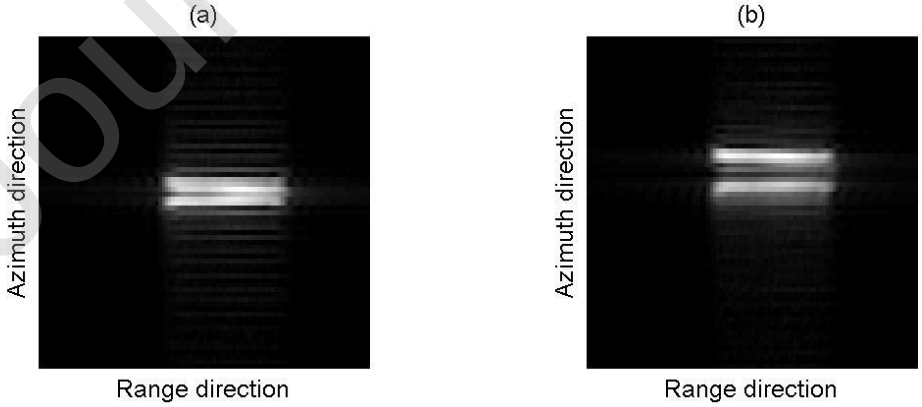

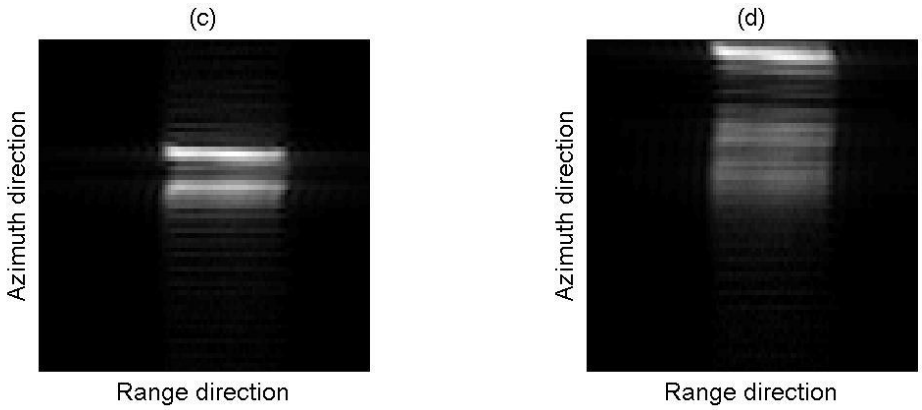

Fig.7. SAL imaging with different ratios of D/r_0 (a) 1/5 (b) 1/2(c) 1/1 (d) 5/1

From Fig.7(a) to Fig.7(d), these are the imaging results with a ratio of real aperture length to atmospheric coherence length. As the ratio increases, the imaging environment becomes harsher.

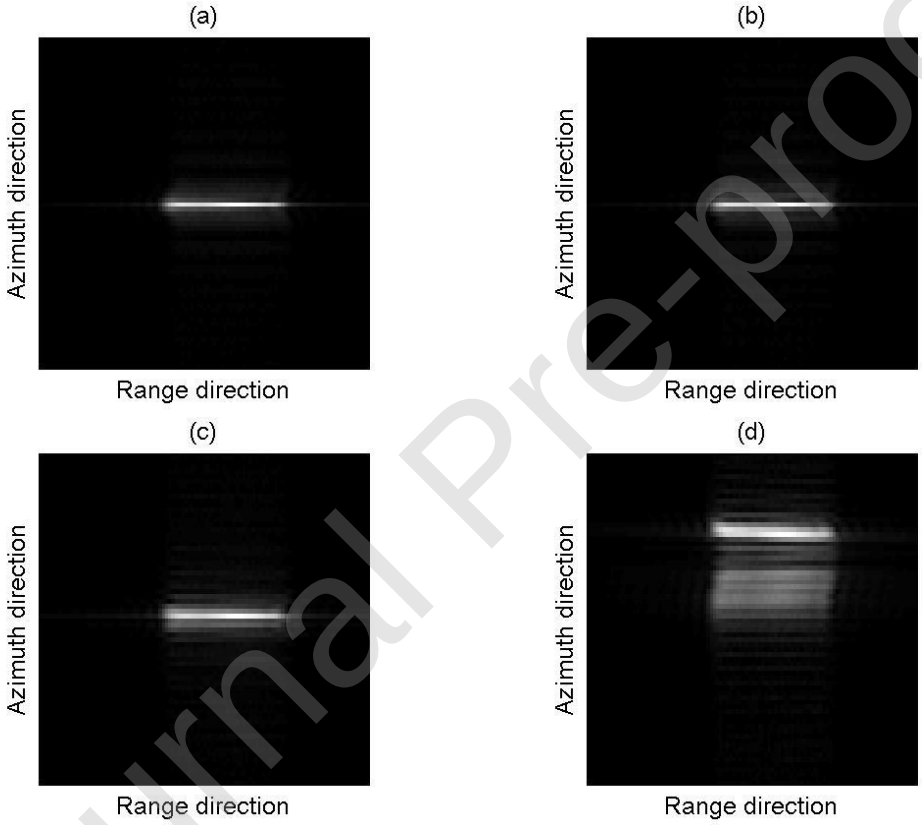

Fig.8. SAL compensation result with different ratios of D/r_0 (a) 1/5 (b) 1/2 (c) 1/1 (d) 5/1

Fig.8 shows the compensation results based on neural networks. Fig.8(a) and Fig.8(b) are the imaging targets with ratio of 1/5 and 1/2, respectively. After 15-time iteration, Targets can be clearly distinguished. Under severe conditions, SAL can not restore the images to the original state, which are shown in Fig.8(c) and Fig.8(d). This tells us the phase errors in echo signals induced by marine atmosphere are irreversible. If atmospheric coherence length is less than real aperture length, only part of them can be compensated.

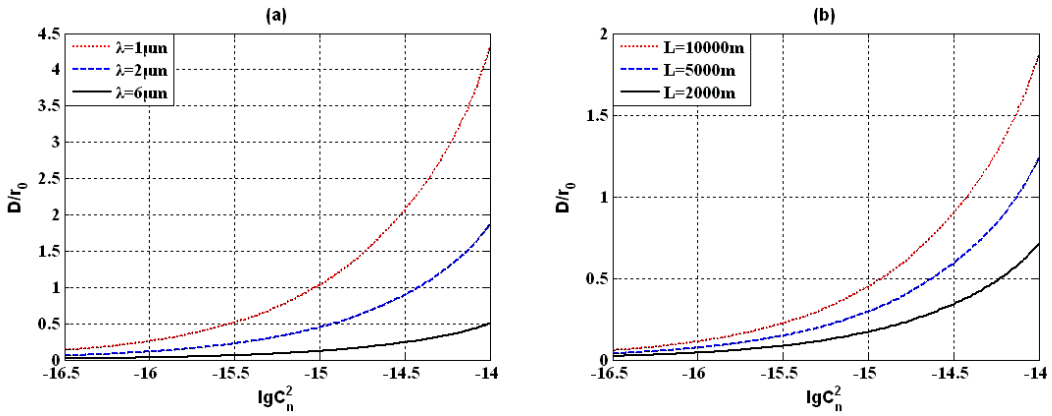

Fig.9. Relation of D/r_0 and turbulence intensity C_n^2 (a) Different wavelengths (b) Different slant ranges

Fig.9 shows the changing law of the ratio with turbulence intensity under different conditions. When D=0.05m, with different wavelengths, as the intensity becomes stronger, the ratio becomes larger, shown in Fig.9(a). When $C_n^2 = 1.0\times10^{-15} m^{-2/3}$, atmospheric coherence length is nearly the same as real aperture length with a wavelength of 1μm. While changing the radiation source to 6μm and $C_n^2 = 1.0\times10^{-14} m^{-2/3}$, the ratio is merely 1/2, that means phase errors can be restored, indicating the advantage of long wavelength. When the wavelength is 2μm, Fig.9(b) shows the influence of slant range growth on the ratio is less than that of wavelength. For instance, although 10000m is five times as 2000m, calculation result illustrates the alleviation of distortion is not significant enough.

5.Conclusion

Based on marine atmospheric power spectrum, this paper combines phase screen and neural network to investigate the turbulence effect on SAL. As the grid number increases, the structure function of phase screens is better consistent with the theoretical value, which examines the accuracy of the method. According to the imaging results under turbulent condition, as turbulence becomes stronger, the defocus effect of images becomes more serious, and better imaging quality will be obtained with a longer laser wavelength. Using neural network based phase screens to preset initial values of the iteration compensation algorithm, when atmospheric coherence length is larger than real aperture length, SAL can focus relatively well. When atmospheric coherence length is smaller than real aperture length, SAL is unable to focus. For SAL imaging, marine atmosphere is an inevitable factor to discuss. In some cases needing higher resolution, we have to lower carrier height above the sea and even use CNN in complex environment to improve SAL imaging quality. This suggestion can also be applied to optical imaging through marine atmosphere.

Declaration of interests

The authors declare that they have no known competing financial interests or personal relationships that could have appeared to influence the work reported in this paper.

Acknowledgements

This work is jointly supported by National Key Research and Development Program of China

(2019YFA0607004) and National Natural Science Foundation of China under Grant Projects No. 41275013 and 41575067.

References

[1] S. M. Beck, J. R. Buck, W. F. Buell, R. P. Dickinson, D. A. Kozlowski, N. J. Marechal, T. J. Wright, Synthetic-aperture imaging laser radar: laboratory demonstration and signal processing, Appl. Opt. 44 (2005) 7621-7629.

[2] Y. Tang, B. Qin, Y. Yan, and M. Xing, Multiple-input multiple-output synthetic aperture ladar system for wide-range swath with high azimuth resolution, Appl. Opt. 55 (2016) 1401-1405.

[3] Andrew J. Stokes, Matthew P. Dierking, David J. Rabb, Interferometric synthetic aperture ladar using code division multiple access apertures, Appl. Opt. 56 (2017) 5003-5012.

[4] G. Li, R. Wang, Z. Song, K. Zhang, Y. Wu, J. Pan, Linear frequency-modulated continuous-wave ladar system for synthetic aperture imaging, Appl. Opt. 56 (2017) 3257-3262.

[5] G. Zhang, J. Sun, Y. Zhou, Z. Lu, G. Li, M. Xu, B. Zhang, C. Lao, H. He, Ghost image in enhanced self-heterodyne synthetic aperture imaging ladar, Opt. Commun. 410 (2018) 591-597.

[6] L. Guo, H. Yin, Y. Zhou, J. Sun, X. Zeng, Y. Tang, M. Xing, A novel sidelobe-suppression algorithm for airborne synthetic aperture imaging ladar, Opt. Laser Technol. 111 (2019) 714-719.

[7] T. J. Karr, Resolution of synthetic-aperture imaging through turbulence, J. Opt. Soc. Am. A 20 (2003) 1067-1083.

[8] B. E. Schumm, M. P. Dierking, Wave optics simulations of synthetic aperture ladar performance through turbulence, J. Opt. Soc. Am. A 34 (2017) 1888-1895.

[9] R. S. Depoy, A. K. Shaw, Algorithm to overcome atmospheric phase errors in SAL data, Appl. Opt. 59 (2020) 140-150.

[10] R. L. Lucke, Synthetic aperture ladar simulations with phase screens and Fourier propagation, in: Proceedings of the IEEE Conference on Aerospace, IEEE, 2004, pp. 1788-1798.

[11] B. Formwalt, S. Cain, Optimized phase screen modeling for optical turbulence, Appl. Opt. 45 (2006) 5657-5668.

[12] F. Dios, J. Recolons, A. Rodríguez, O. Batet, Temporal analysis of laser beam propagation in the atmosphere using computer-generated long phase screens, Opt. Express16 (2008) 2206-2220.

[13] I. Toselli, O. Korotkova, X. Xiao, D. G. Voelz, SLM-based laboratory simulations of Kolmogorov and non-Kolmogorov anisotropic turbulence, Appl. Opt. 54 (2015) 4740-4744.

[14] D. A. Paulson, C. Wu, C. C. Davis, Randomized spectral sampling for efficient simulation of laser propagation through optical turbulence, J. Opt. Soc. Am. B36 (2019) 3249-3262.

[15] P. Lochab, P. Senthilkumaran, K. Khare, Propagation of converging polarization singular beams through atmospheric turbulence, Appl. Opt. 58 (2019) 6335-6345.

[16] K. J. Grayshan, F. S. Vetelino, C. Y. Young, A marine atmospheric spectrum for laser propagation, Wave Random Media 18 (2008) 173–184.

[17] Y. Baykal, Higher-order laser beam scintillation in weakly turbulent marine atmospheric medium, J. Opt. Soc. Am. A 33 (2016) 758-763.

[18] Y. Xu, Y. Zhu, Y. Zhang, Crosstalk probability of the bandwidth-limited orbital angular momentum mode of Bessel Gaussian beams in marine-atmosphere turbulence, Opt. Commun. 427 (2018) 493-496.

[19] S. Lohani, E. M. Knutson, M. O'Donnell, S. D. Huver, R. T. Glasser, On the use of deep neural networks in optical communications, Appl. Opt.57 (2018) 4180-4190.

[20] S. Lohani, R. T. Glasser, Turbulence correction with artificial neural networks, Opt. Lett. 43 (2018) 2611-2614.

[21] J. Liu, P. Wang, X. Zhang, Y. He, X. Zhou, H.Ye, Y. Li, S. Xu, S. Chen, D. Fan, Deep learning based atmospheric turbulence compensation for orbital angular momentum beam distortion and communication, Opt. Express 27 (2019) 16671-16688.

[22] Q. Zhao, S. Hao, Y. Wang, L. Wang, C. Xu, Orbital angular momentum detection based on diffractive deep neural network, Opt. Commun. 443 (2019) 245-249.

[23] Y. Liu, S. Zhang, J. Suo, T. Yao, J. Zhang, Research on Cognitive Marine Radar Based on LFM Waveform Control, Sensors 19 (9) (2019) 2200-2217.

[24] T. Matos, C. L. Faria, M. S. Martins, R. Henriques, P. A. Gomes, L. M. Goncalves, Development of a Cost-Effective Optical Sensor for Continuous Monitoring of Turbidity and Suspended Particulate Matter in Marine Environment, Sensors 19 (20) (2019) 4439-4459.

[25] C. Do, T. T. D. Nguyen, W. Liu, Tracking Multiple Marine Ships via Multiple Sensors with Unknown Backgrounds, Sensors 19 (22) (2019) 5025-5039.

[26] D. M. Brown, J. C. Juarez, A. M. Brown, Laser differential image-motion monitor for characterization of turbulence during free-space optical communication tests, Appl. Opt. 52 (2013) 8402-8410.

[27] M. Li, M. Cvijetic, Y. Takashima, Z. Yu, Evaluation of channel capacities of OAM-based FSO link with real-time wavefront correction by adaptive optics, Opt. Express 22 (2014) 31337-31346.

[28] I. Naeh, A. Katzir, Perfectly correlated phase screen realization using sparse spectrum harmonic augmentation, Appl. Opt. 53 (2014) 6168-6174.

[29] C. A. Snarski, Rank one phase error estimation for range-Doppler imaging, IEEE Trans. Aerospace Electron. Syst. 32 (2) (1996) 676-688.

[30] P. H. Eichel, C. V. Jakowatz, Phase-gradient algorithm as an optimal estimator of the phase derivative, Opt. Lett. 14 (1989) 1101-1103.

[31] S. Crouch, Z. W. Barber, Laboratory demonstrations of interferometric and spotlight synthetic aperture ladar techniques, Opt. Express 20 (2012) 24237-24246.

[32] Z. W. Barber, J. R. Dahl, Synthetic aperture ladar imaging demonstrations and information at very low return levels, Appl. Opt. 53 (2014) 5531-5537.